Comparison and Assessment of some Synthetic Jet Models

Régis Duvigneau, Jérémie Labroquère

Comparison and Assessment of some Synthetic Jet Models

Régis Duvigneau, Jérémie Labroquère

RESEARCH REPORT
N° 8409
December 2013
Project-Team Opale

ISSN 0249-6399 ISRN INRIA/RR--8409--FR+ENG

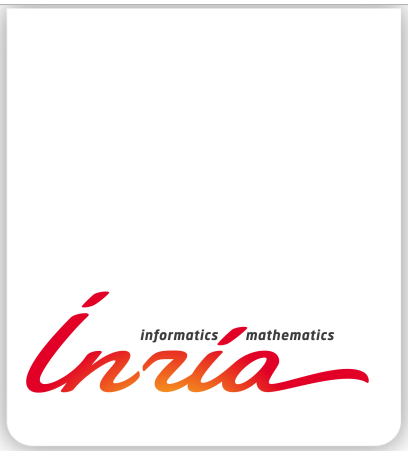

Comparison and Assessment of some Synthetic Jet Models

Régis Duvigneau*, Jérémie Labroquère*

Project-Team Opale

Research Report n° 8409 — December 2013 — 40 pages

Abstract: A synthetic jet is an oscillatory jet, with zero time-averaged mass-flux, used to manipulate boundary layer characteristics for flow control applications such as drag reduction, detachment delay, etc. The objective of this work is the comparison and assessment of some numerical models of synthetic jets, in the framework of compressible flows governed by Reynolds-averaged Navier-Stokes (RANS) equations. More specifically, we consider three geometrical models, ranging from a simple boundary condition, to the account of the jet slot and the computation of the flow in the underlying cavity. From numerical point of view, weak and strong oscillatory boundary conditions are tested. Moreover, a systematic grid and time-step refinement study is carried out. Finally, a comparison of the flows predicted with two turbulence closures (Spalart-Allmaras and Menter SST $k-\omega$ models) is achieved.

Key-words: synthetic jet, boundary condition, turbulence, RANS

* Opale Project-Team

RESEARCH CENTRE
SOPHIA ANTIPOLIS – MÉDITERRANÉE

2004 route des Lucioles - BP 93
06902 Sophia Antipolis Cedex

Comparaison et validation de quelques modèles de jet synthétique

Résumé : Un jet synthétique est un jet oscillant, avec un flux de masse nul en moyenne temporelle, utilisé pour manipuler les caractéristiques de couche limite pour des applications au contrôle d'écoulement, comme la réduction de traînée, le retard de décollement, etc. L'objectif de ce travail est de comparer et valider quelques modèles numériques de jets synthétiques, dans le cadre d'écoulements compressibles gouvernés par les équations de Navier-Stokes en moyenne de Reynolds (RANS). Plus spécifiquement, on considère trois modèles géométriques, allant d'une simple condition aux limites, à la prise en compte de la fente du jet et le calcul de l'écoulement dans la cavité sous-jacente. Du point de vue numérique, des conditions aux limites oscillantes faibles et fortes sont testées. De plus, une étude de raffinement systématique du maillage et du pas de temps est réalisée. Finalement, on compare les écoulements prédits avec deux fermetures turbulentes (modèles de Spalart-Allmaras et $k-\omega$ SST de Menter).

Mots-clés : jet synthétique, condition aux limites, turbulence, RANS

1 Introduction

Flow control is an active research area for the last decade, which benefits from the progress of simulation methods in terms of accuracy and robustness, and from the continuous increase of computational facilities. Actuator devices, such as synthetic jets or vortex generators, have proved their ability to modify the flow dynamics and represent a promising way to improve the aerodynamic performance of a system, without modifying its shape. However, the determination of efficient flow control parameters, in terms of location, frequency, amplitude, etc., is tedious and highly problem dependent [7, 11].

To overcome this issue, the numerical simulation of controlled flows is often considered to determine optimal control parameters, or at least a range of efficient parameters. This task can be carried out in a systematic and parametric way [11], but the use of an automated optimization procedure is more and more observed [2, 3, 9, 13, 19]. However, several studies have shown that the simulation of controlled flows is a difficult task, because of the presence of complex turbulent structures. Large Eddy Simulation (LES) is certainly the most appropriate approach for such problems [5], but the related computational burden makes its use tedious for optimization or exploration of control parameters. Reynolds-Averaged Navier-Stokes (RANS) models are more suitable in practice, but the results obtained may be highly dependent on the turbulence closure used. Moreover, the numerical assessment should be done carefully because the solution is strongly influenced by the numerical parameters, such as the time step or the grid size. As consequence, the simulation results exhibit modeling and numerical errors, which may lead the optimization process to failure, or to unexpected low efficiency [8].

Therefore, this study is intended to provide a rigorous and systematic assessment of some actuators models, and quantify the impact of the turbulence closures and numerical parameters, as a preparatory phase before optimization of the control laws.

The first part of the report describes the numerical framework of the study and the actuator models studied. Then, the selected test-case is presented. Finally, the results obtained are analyzed, in terms of impact of the actuator model, impact of the numerical parameters, impact of discretization level and impact of the turbulence closure.

2 Numerical framework

2.1 Discretization

The compressible flow analysis is performed using the NUM3SIS platform developed at INRIA Sophia-Antipolis (see `http://num3sis.inria.fr`). For this study, we consider the two-dimensional Favre-averaged Navier-Stokes equations, that can be written in the conservative form as follows:

$$\frac{\partial \mathbf{W}}{\partial t} + \frac{\partial \mathbf{F}_1(\mathbf{W})}{\partial x} + \frac{\partial \mathbf{F}_2(\mathbf{W})}{\partial y} = \frac{\partial \mathbf{G}_1(\mathbf{W})}{\partial x} + \frac{\partial \mathbf{G}_2(\mathbf{W})}{\partial y}, \tag{1}$$

where $\mathbf{W}$ are the conservative mean flow variables $(\rho, \rho u, \rho v, E)$, with ρ the density, $\vec{U} = (u, v)$ the velocity vector and E the total energy per unit of volume. $\vec{F} = (\mathbf{F}_1(\mathbf{W}), \mathbf{F}_2(\mathbf{W}))$ is the vector of the convective fluxes and $\vec{G} = (\mathbf{G}_1(W), \mathbf{G}_2(W))$ the vector of the diffusive fluxes. The pressure p is obtained from the perfect gas state equation $p = (\gamma - 1)(E - \frac{1}{2}\rho \| \overrightarrow{U} \|^2)$ where $\gamma = 1.4$ is the ratio of the specific heat coefficients.

Provided that the flow domain Ω is discretized by a triangulation $\mathcal{T}_h$, a discretization of equation (1) at the mesh node s_i is obtained by using a mixed finite-volume / finite-element formulation [6, 14]. The finite-volume cell C_i is built around the node s_i by joining the midpoints of the edges adjacent to s_i to some points inside the triangles containing s_i. The latter points could be the barycenter of the triangles in the case of rather isotropic cells, or the orthocenter in the case of anisotropic cells, as in the boundary layers, to avoid the definition of stretched cells. Finite-elements correspond to classical P1 elements constructed on each triangle. Finally, the following semi-discretized form is obtained:

$$Vol_i \frac{\partial \mathbf{W}_i}{\partial t} + \sum_{j \in N(i)} \Phi(\mathbf{W}_i, \mathbf{W}_j, \overrightarrow{\sigma}_{ij}) = \sum_{k \in E(i)} \Psi_k, \tag{2}$$

where $\mathbf{W}_i$ represents the cell-averaged state and Vol_i the volume of the cell C_i. $N(i)$ is the set of the neighboring vertices and $E(i)$ the set of the neighboring triangles. $\Phi(\mathbf{W}_i, \mathbf{W}_j, \overrightarrow{\sigma}_{ij})$ is an approximation of the integral of the convective fluxes over the boundary ∂C_{ij} between C_i and C_j, which depends on $\mathbf{W}_i$, $\mathbf{W}_j$ and $\overrightarrow{\sigma}_{ij}$ the integral of a unit normal vector over ∂C_{ij}. The convective fluxes are evaluated using upwinding, according to the approximate HLLC Riemann solver [1]. A high-order scheme is obtained by reconstructing the physical variables at the midpoint of $[s_i s_j]$ using $\mathbf{W}_i$, $\mathbf{W}_j$ and the upwind gradient (β-scheme), before the fluxes are evaluated. Ψ_k is the contribution of the triangle k to the diffusive terms, according to a classical P1 description of the flow fields.

The inlet and outlet boundary conditions are imposed weakly, using a modified Steger-Warming flux [6], whereas the no-slip boundary condition at the wall is strongly enforced by an implicit condition.

An dual time-stepping procedure is used for the time integration of (2). For the physical time, a classical three-step backward scheme ensures a second-order accurate discretization. An implicit first-order backward scheme is employed to solve the resulting non-linear problem at each time-step. The linearization of the numerical fluxes yields the following integration scheme:

$$\left((\frac{Vol_i}{\Delta t} + \frac{Vol_i}{\Delta \tau})\, Id + J_i^p \right) \delta \mathbf{W}_i^{p+1} = - \sum_{j \in N(i)} \Phi_{ij}^p + \sum_{k \in E(i)} \Psi_k^p - \frac{3}{2}\frac{Vol_i}{\Delta t}\delta \mathbf{W}_i^n + \frac{1}{2}\frac{Vol_i}{\Delta t}\delta \mathbf{W}_i^{n-1} \tag{3}$$

with:

$$\delta \mathbf{W}_i^{p+1} = (\mathbf{W}_i^{n+1})^{p+1} - (\mathbf{W}_i^{n+1})^p \qquad \delta \mathbf{W}_i^{n} = (\mathbf{W}_i^{n+1})^{p} - \mathbf{W}_i^{n} \qquad \delta \mathbf{W}_i^{n-1} = \mathbf{W}_i^{n} - \mathbf{W}_i^{n-1} \quad (4)$$

J_i^p is the Jacobian matrix of the convective and diffusive terms and $\Delta\tau$ is the pseudo time-step. For the computation of the convective Jacobian, we employ the first-order flux of Rusanov [14], while the Jacobian of the diffusive terms is computed exactly. The right hand side of (3) is evaluated using high order approximations. The resulting integration scheme provides a second-order solution in space and time. The linear system is inverted using the GMRES method, including an ILU preconditionner.

2.2 Turbulence closures

Two linear eddy-viscosity models are used in this study, namely the Spalart-Allmaras and Menter SST $k-\omega$ models, which are commonly employed for industrial problems.

The Spalart-Allmaras model is a one-equation closure calibrated on simple flows, which is intensively used in aerodynamics. It provides satisfactory results on attached flows and gives a better description of velocity fields for detached flows than zero-equation models. Several versions and variants of this model, including curvature corrections, have been developed since the original version was written. The details are not described here, but the implemented compressible version [10] corresponds to the standard model.

The k-ω model is a two-equation turbulence closure. It is based on the transport equations of the turbulent kinetic energy k and the characteristic frequency of the largest eddies ω. It is well known that the simple k-ω closure is sensitive to boundary conditions, but can be integrated to the wall. This drawback is alleviated by the SST (Shear Stress Transport) k-ω model from Menter [16], which is far more employed now. The domain of validity of the latter model is larger than the Spalart-Allmaras one, but it is still limited by the linear Boussinesq assumption.

From numerical point of view, the additional transport equations for turbulent variables are discretized using similar principles as the equations for the mean-flow variables. They are treated in a segregated way, by solving the equations for turbulent variables with frozen flow variables, and vice-versa.

3 Synthetic jet models

A synthetic jet is a fluidic actuator that injects momentum in the boundary layer by the mean of oscillatory blowing and suction phases. It has been found efficient for flow vectorization, mixing enhancement or detachment delay [12, 17, 18]. This actuator is especially interesting for real-life flow control problems, because it is compact and does not require air supply, contrary to pulsated jets for instance.

As illustrated in the previous references, practical synthetic jets can be of different types. Nevertheless, they are usually composed of a cavity with a moving surface, which generates inflow and outflow though a slot, as shown in Fig. (1). The numerical simulation of a synthetic jet in interaction with the flow in the outer domain is tedious, for several reasons. If one intends to represent exactly the device, the simulation of the flow in the deformable cavity should be

achieved, which requires to use sophisticated methods like automated grid deformation, ALE (Arbitrary Lagrangian Eulerian) formulation, etc. Moreover, a significant part of the computational time could be devoted to the simulation of the flow inside the cavity, which is usually not the main purpose. Obviously, the introduction of the actuator makes the grid generation step more complex and the automatization of the process could be tedious, if possible. This is especially dommageable in a design optimization framework, if one intends to optimize the actuator location, for instance. These reasons motivate the development and the use of simplified models in an industrial context. Some of them are detailed below.

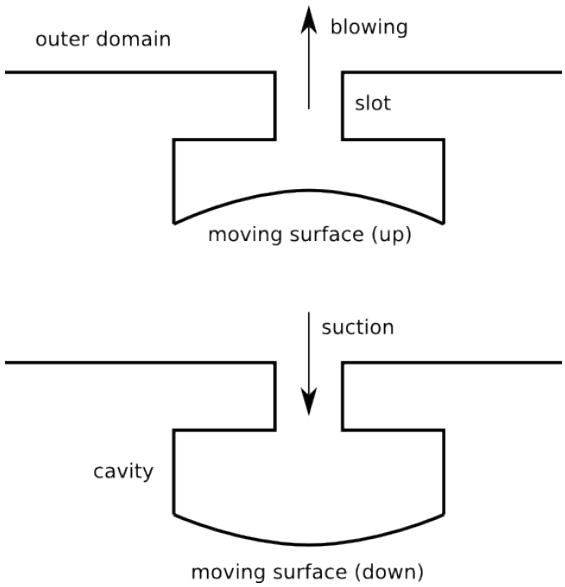

Figure 1: Synthetic jet principle.

3.1 Cavity model

A first simplification consists in using a fixed computational domain. In that case, the move of the bottom surface of the cavity is modeled by imposing a prescribed boundary condition for the flow velocity [5] and possibly for the normal pressure gradient [15], as illustrated by Fig. (2).

In this study, we impose the value of the velocity at the bottom surface, as:

$$\vec{U} = U_c A_c(\xi_c) \sin(2\pi f t)\ \vec{\eta_c} \tag{5}$$

where U_c is the oscillation amplitude of the velocity at the cavity bottom surface, (ξ_c, η_c) a local frame system and f is the actuation frequency. $A_c(\xi_c)$ describes the velocity profile along the surface, which is here defined as:

$$A_c(\xi_c) = \sin^2\left(2\pi \frac{\xi_c - \xi_c^{min}}{\xi_c^{max} - \xi_c^{min}}\right) \tag{6}$$

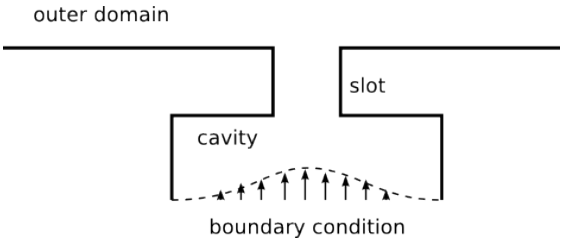

Figure 2: Cavity model.

where ξ_c^{max} and ξ_c^{min} are the maximum and minimum abscissae of the boundary considered (bottom cavity). Thus, the actuation is finally defined by the two parameters (U_c, f).

Practically, this boundary condition can be implemented in several ways. A first (weak) approach consists in imposing the velocity value (5) during the computation of the numerical flux at the boundary. Other variables used for the flux definition are computed from the interior of the computational domain. An alternate (strong) approach consists in imposing the value of the velocity field itself, by modifying the linear system (3) to verify implicitly the condition (5).

3.2 Slot model

The major drawback of the cavity model is related to the computational time used to simulate the flow inside the cavity, which is usually not negligible due to the necessity to use a refined grid in the cavity. Therefore, a second simplification level consists in replacing the cavity by a simple boundary condition located at the slot extremity, as illustrated by Fig. (3). This shortcut reduces the computational burden, but does not allow to describe the flow in the cavity and the possible Helmholtz resonance phenomenon that can occur inside [4].

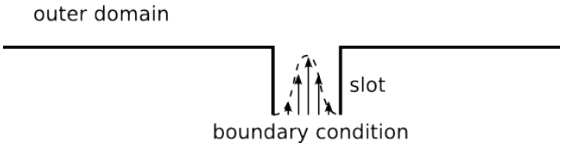

Figure 3: Slot model.

The boundary condition is formally equivalent to (6), but with different parameters:

$$\vec{U} = U_s A_s(\xi_s) \sin(2\pi f t)\ \vec{\eta_s} \tag{7}$$

$$A_s(\xi_s) = \sin^2\left(2\pi \frac{\xi_s - \xi_s^{min}}{\xi_s^{max} - \xi_s^{min}}\right) \tag{8}$$

The local frame (ξ_s, η_s) is now attached to the bottom slot surface. ξ_s^{max} and ξ_s^{min} are the maximum and minimum abscissae of the boundary considered (bottom slot). To impose an

equivalent flow rate, the following relationship should be verified:

$$U_s = U_c \, \frac{\xi_c^{max} - \xi_c^{min}}{\xi_s^{max} - \xi_s^{min}} \tag{9}$$

The practical implementation of the boundary condition is exactly the same as the one used for the cavity model.

3.3 Boundary condition model

Finally, the simplest model just consists in imposing a boundary condition for the velocity at the slot exit, as illustrated by Fig. (4). This model makes the grid generation process slightly easier, but the benefit is not significant, because the mesh should anyway account for the jet, as shown in the following numerical study. This model does not allow to describe the interaction between the flow in the outer domain and the flow exiting the slot. However, this model is certainly the most used in the literature due to its implementation ease.

Figure 4: Boundary model.

In practice, the boundary condition is the same as previously, defined by (7-8).

4 Test-case description

To compare the flows predicted by the different models and quantify the impact of the numerical parameters, we consider as test-case a single synthetic jet located on a flat plate and interacting with a boundary layer, as illustrated by Fig. (5). The baseline case, without actuator, corresponds to the zero pressure gradient flat plate verification case proposed by NASA and fully defined at `http://turbmodels.larc.nasa.gov/flatplate.html`. The plate length is 2 m, whereas the computational domain height is 30 cm. The distance between the inlet boundary and the plate is 40 cm, and the distance between the stagnation point and the jet center is 50.25 cm. The slot width measures $h = 5$ mm. The length of the slot is twice its width $2h$. The cavity dimension is $9h \times h$.

The reference flow conditions are the following :

ρ_{ref}	1.363 kg/m^3
u_{ref}	69.437 m/s
p_{ref}	115056 Pa
μ_{ref}	$1.9\,10^{-5}$ Pa s

The resulting Mach and Reynolds numbers are respectively $M_{ref} = 0.2$ and $Re_{ref} = 5\,10^6$. Note that the resulting boundary layer thickness at the actuation location is about twice the slot width. A validation of the flow simulation without actuation is first achieved, in terms of skin friction coefficient and velocity profile by comparing with experiments and other codes, as

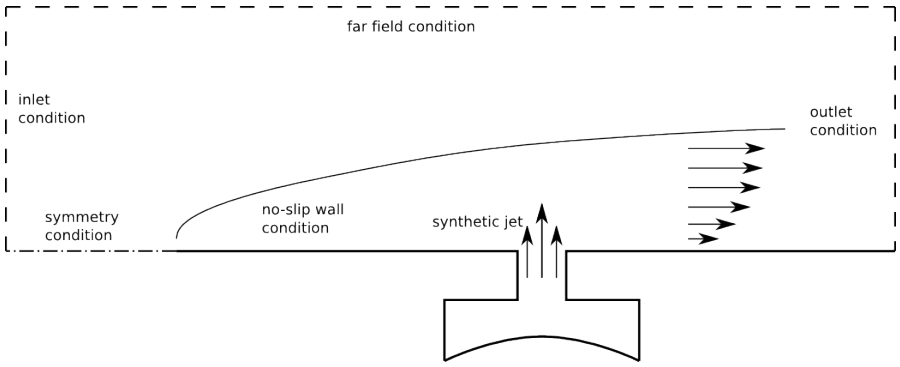

Figure 5: Test-case description.

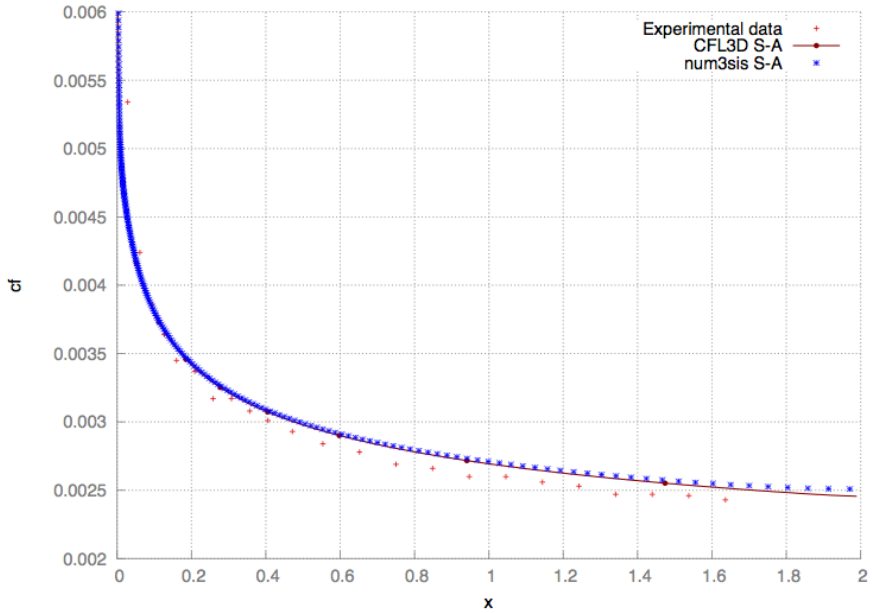

Figure 6: Comparison of the friction coefficient along the plate (without actuation).

illustrated by Figs. (6-7) for the Spalart-Allmaras model.

All inlet / outlet boundary conditions are imposed weakly. At the inlet boundary, the velocity value u_{ref} and density ρ_{ref} are imposed, while the pressure is computed from the interior domain. On the contrary, an imposed pressure condition of value p_{ref} is prescribed at the outlet boundary. For the far-field condition, boundary values are computed thanks to Riemann invariants.

Two sets of actuation parameters are tested. The first one corresponds to a rather low frequency - low amplitude actuation, whereas the second one exhibits high frequency - high

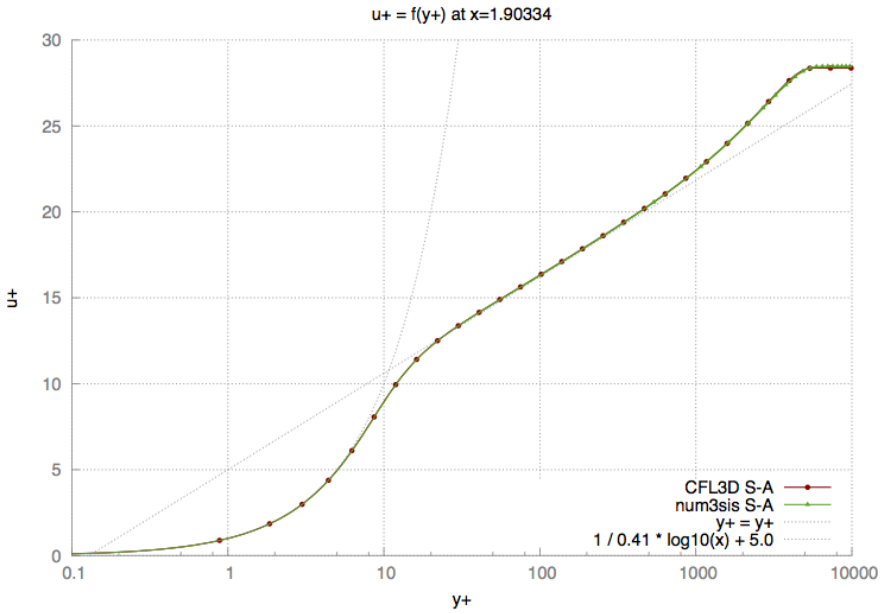

Figure 7: Comparison of the velocity profiles at outlet (without actuation).

amplitude characteristics:

Actuation 1	$f = 50$ Hz	$Us = U_{ref}/2 = 34.72$ m/s
Actuation 2	$f = 500$ Hz	$Us = 2\,U_{ref} = 138.87$ m/s

For all the computations below, the time-step is chosen to account for 200 steps for each actuation period. Therefore, the time-step is defined as $\Delta t_1 = 1.\,10^{-4}$ s for the first actuation, and $\Delta t_2 = 1.\,10^{-5}$ s for the second one. The unsteady simulations are initialized by the steady state solutions corresponding to the flows without actuation. For each time-step, a stopping criterion corresponding to a reduction of 3 orders of the non-linear residuals is adopted.

The baseline grids used for the three models are depicted on Figs. (5-11) and count $N_c = 36848$, $N_s = 19304$ and $N_b = 17424$ vertices respectively, for the cavity model, the slot model and the boundary model respectively. The maximal aspect ratio of the cells is about 40000. The number of vertices located on the jet exit is 40. Note that the grids are identical in the outer domain.

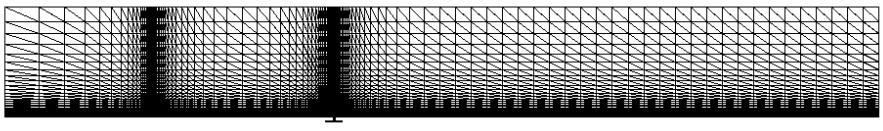

Figure 8: Global view of the mesh.

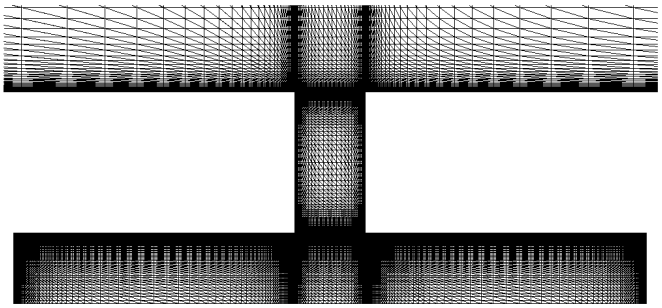

Figure 9: Mesh in the vicinity of the actuator, cavity model.

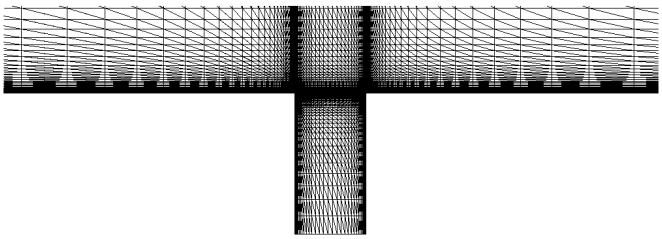

Figure 10: Mesh in the vicinity of the actuator, slot model.

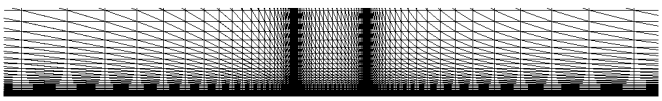

Figure 11: Mesh in the vicinity of the actuator, boundary model.

5 Comparison of the synthetic jet models

Computations are carried out until a periodic flow is observed. Comparisons of the two velocity components for the three models, in the vicinity of the actuator, are provided by Figs. (12-19) for the first actuation, and by Figs. (20-27) for the second actuation. On these figures, the phase $\Phi = 0$ corresponds to the maximum blowing time and $\Phi = \pi$ to the maximum suction time. The SST $k - \omega$ turbulence closure is used here.

Clearly, the flows obtained using the three models are close to each other. The boundary model generates obviously a more symmetric flow at the slot exit, due to the boundary condition on the velocity. The slot and the cavity models allow to compute the flow in the slot, which is characterized by strong asymmetry and generates a more intense flow at the slot corners. One can notice that the cavity and slot models only differ at the bottom part of the slot, with a negligible influence on the flow in the outer domain. The second actuation, with high frequency and amplitude, exhibits larger discrepancies.

A comparison of the drag coefficient is also performed, as a more global assessment criterion. Fig. (28) confirms that the cavity and boundary models predict very similar flows, whereas the boundary model slightly underestimates the drag coefficient value, especially for the second actuation parameters.

The conclusions of these comparisons are the following: although the cavity model is far more CPU-demanding than the slot model, the discrepancy between the two predicted flows is weak, in terms of local field values and global drag coefficient. The boundary model predicts similar flows. However, some differences are reported for high-frequency high-amplitude actuation. In the perspective of more complex studies, the slot model seems to be the best compromise, in terms of CPU cost and flow prediction. An alternate approach could be to capture the velocity profile computed at the slot exit using the cavity model, and use it as boundary condition for the boundary model. However, if one considers a jet with varying parameters (amplitude, frequency, location), it is not clear that the selected profile will correspond to the new conditions. For these reasons, the boundary model could be considered as reasonable for design optimization purpose, provided that actuation characteristics are moderate.

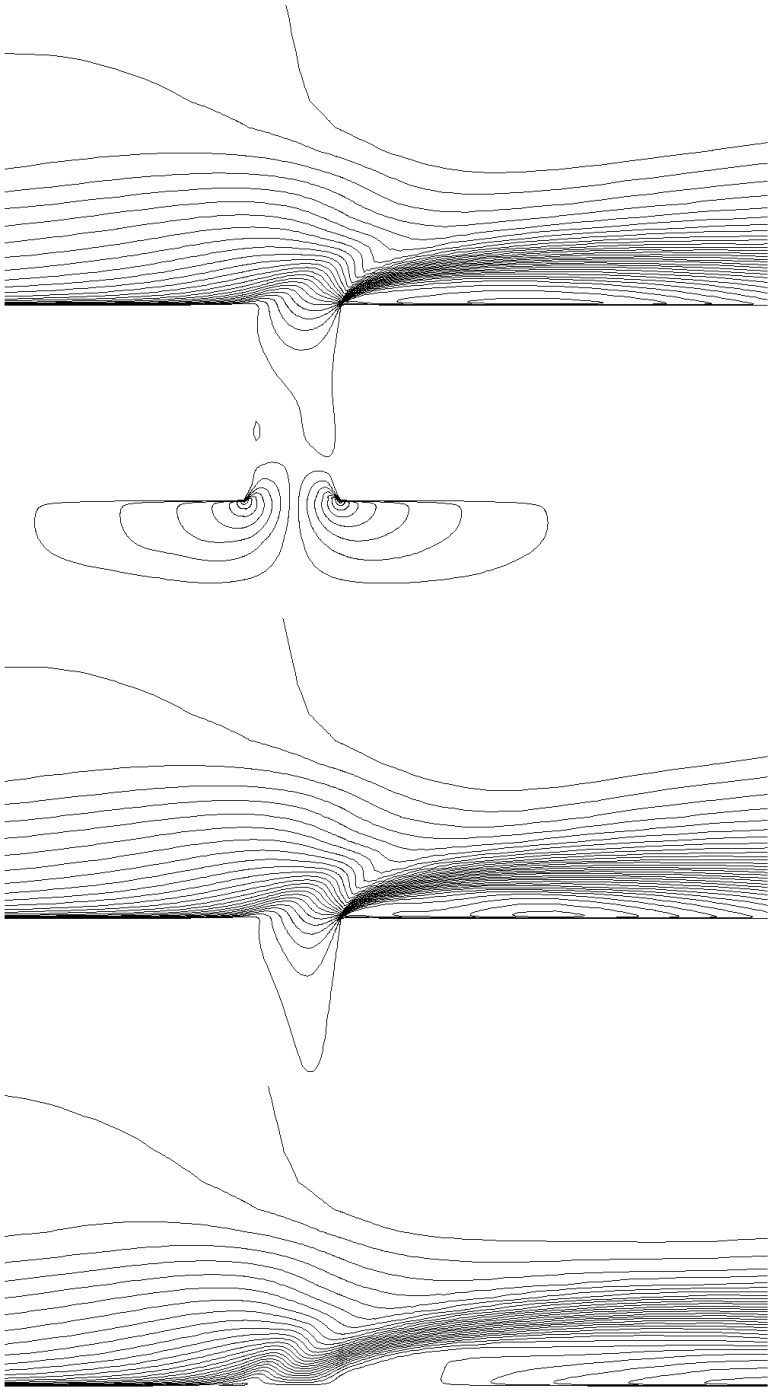

Figure 12: Iso-u contours for the cavity (top), slot (middle) and boundary (bottom) models, for $\Phi = 0$ (50 Hz).

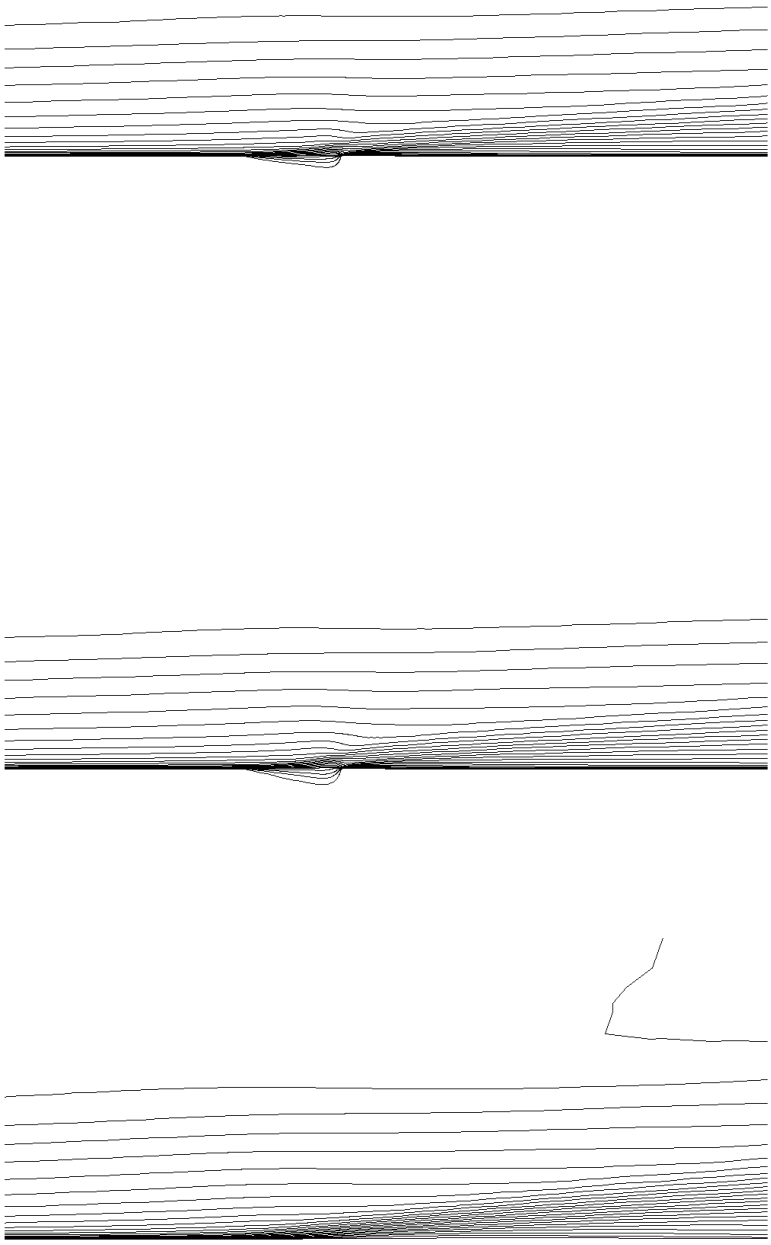

Figure 13: Iso-u contours for the cavity (top), slot (middle) and boundary (bottom) models, for $\Phi = \pi/2$ (50 Hz).

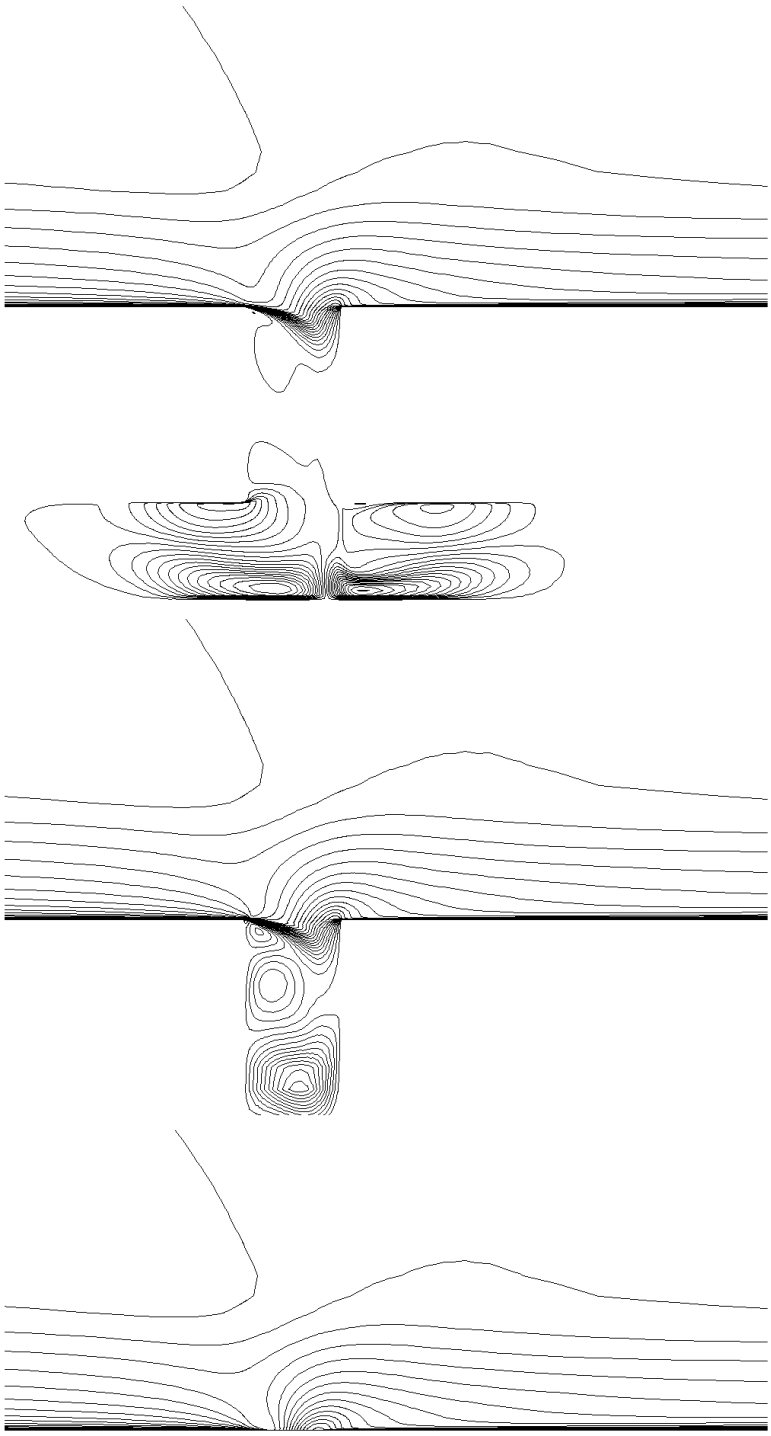

Figure 14: Iso-u contours for the cavity (top), slot (middle) and boundary (bottom) models, for $\Phi = \pi$ (50 Hz).

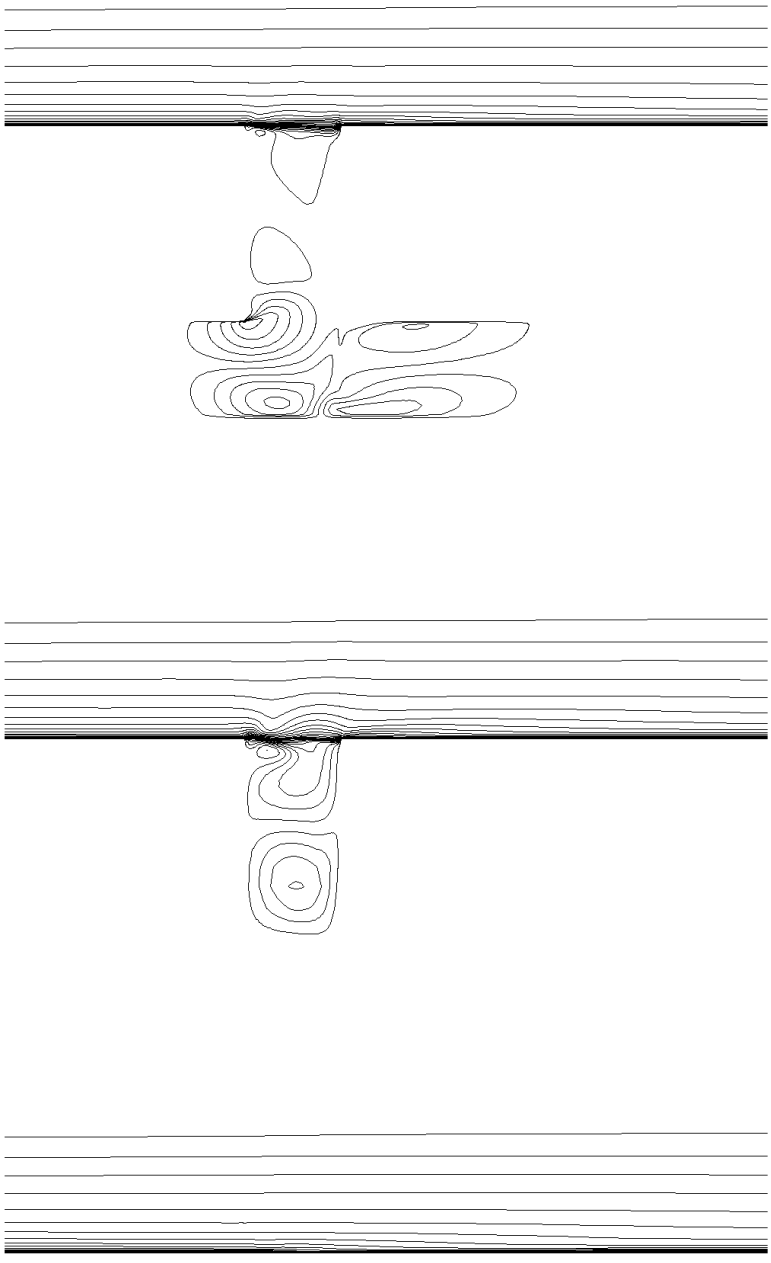

Figure 15: Iso-u contours for the cavity (top), slot (middle) and boundary (bottom) models, for $\Phi = 3\pi/2$ (50 Hz).

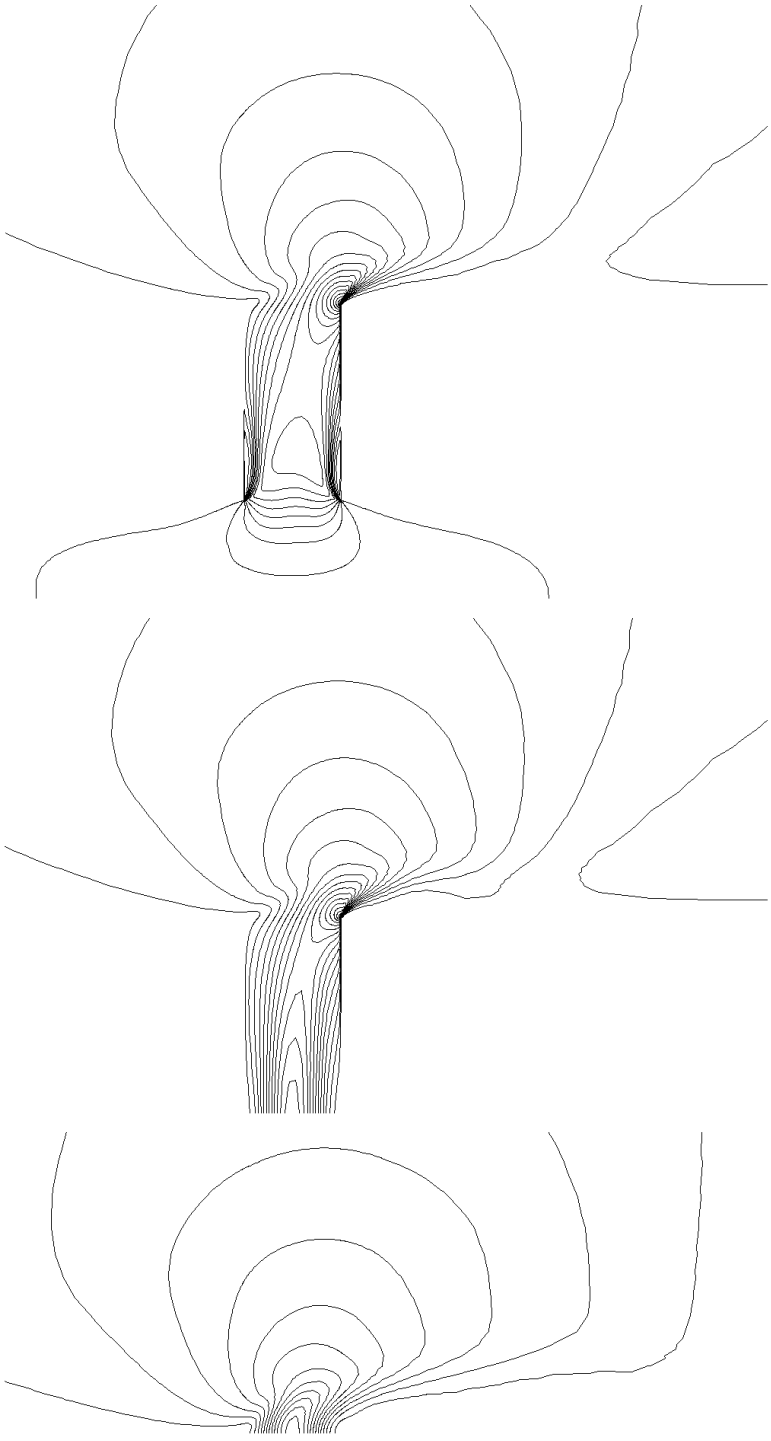

Figure 16: Iso-v contours for the cavity (top), slot (middle) and boundary (bottom) models, for $\Phi = 0$ (50 Hz).

Figure 17: Iso-v contours for the cavity (top), slot (middle) and boundary (bottom) models, for $\Phi = \pi/2$ (50 Hz).

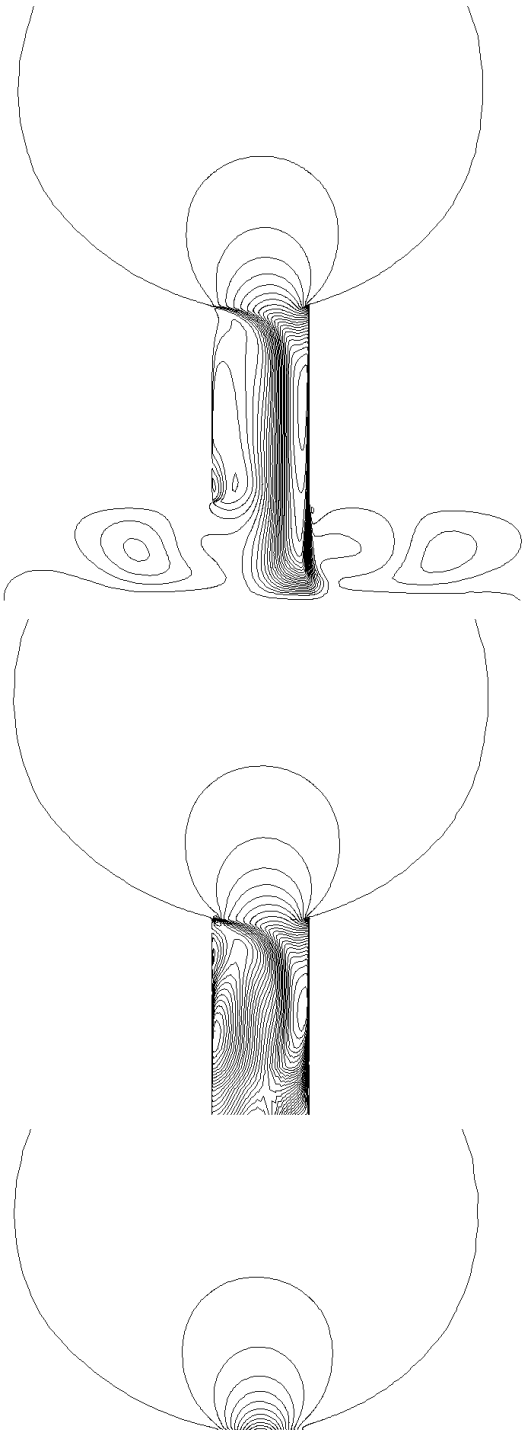

Figure 18: Iso-v contours for the cavity (top), slot (middle) and boundary (bottom) models, for $\Phi = \pi$ (50 Hz).

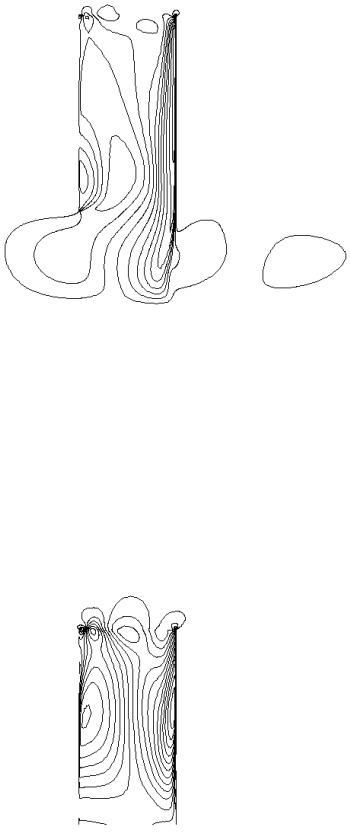

Figure 19: Iso-v contours for the cavity (top), slot (middle) and boundary (bottom) models, for $\Phi = 3\pi/2$ (50 Hz).

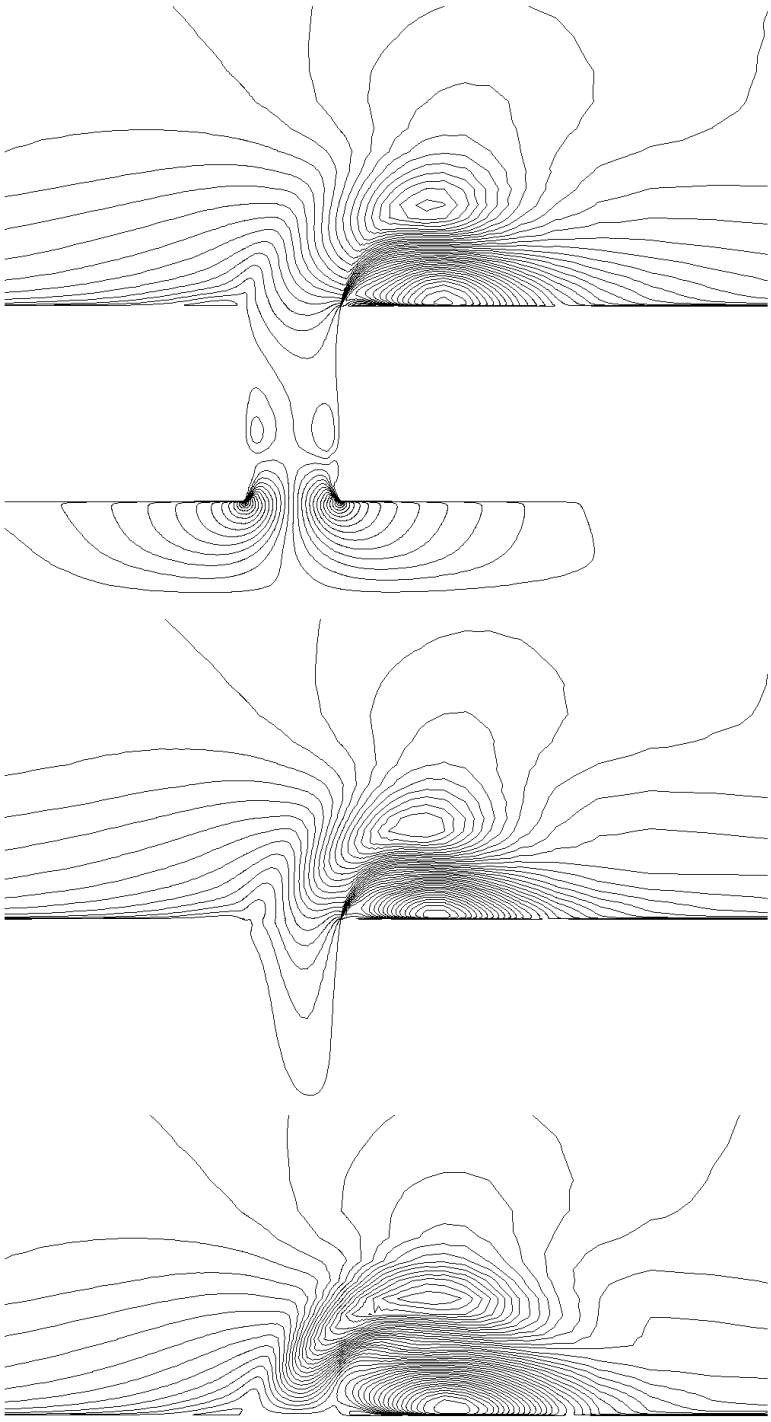

Figure 20: Iso-u contours for the cavity (top), slot (middle) and boundary (bottom) models, for $\Phi = 0$ (500 Hz).

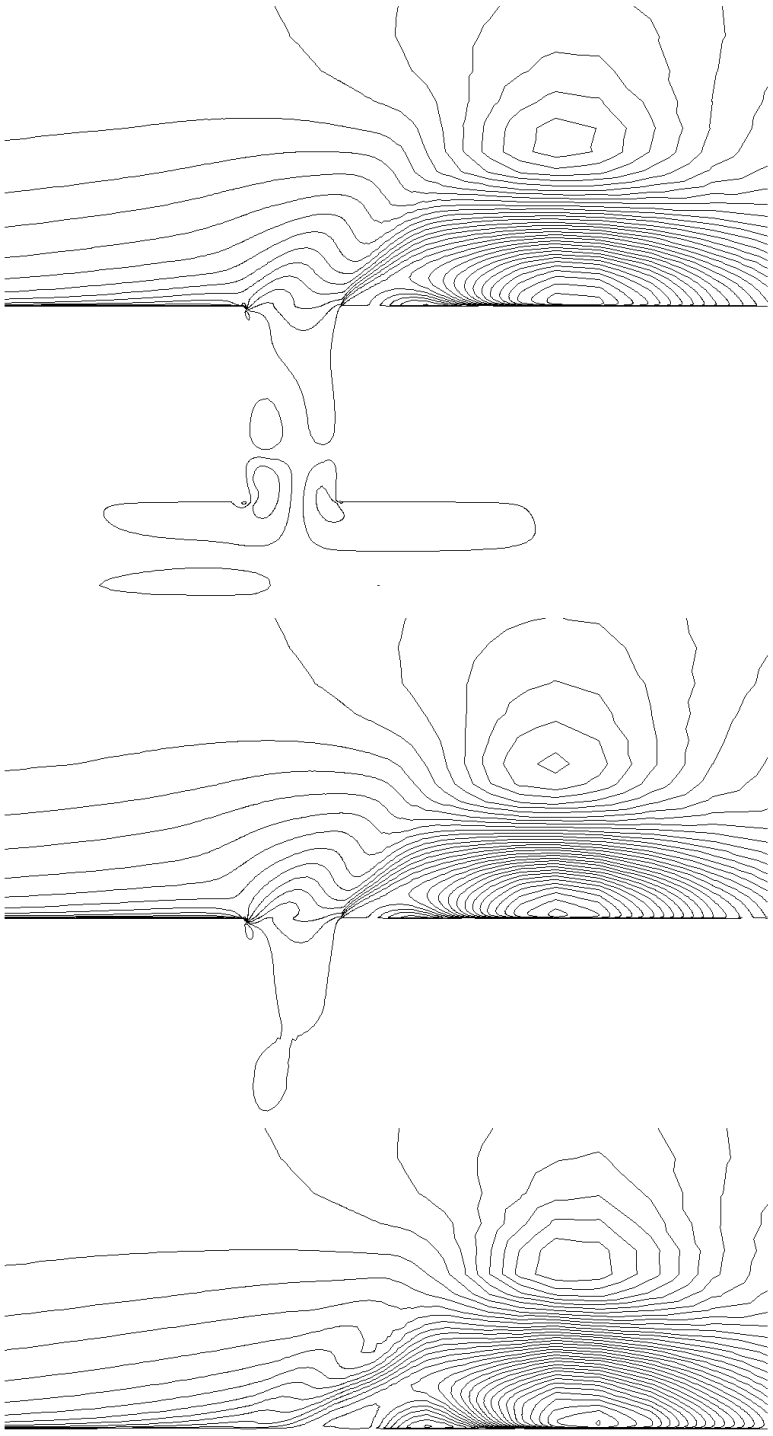

Figure 21: Iso-u contours for the cavity (top), slot (middle) and boundary (bottom) models, for $\Phi = \pi/2$ (500 Hz).

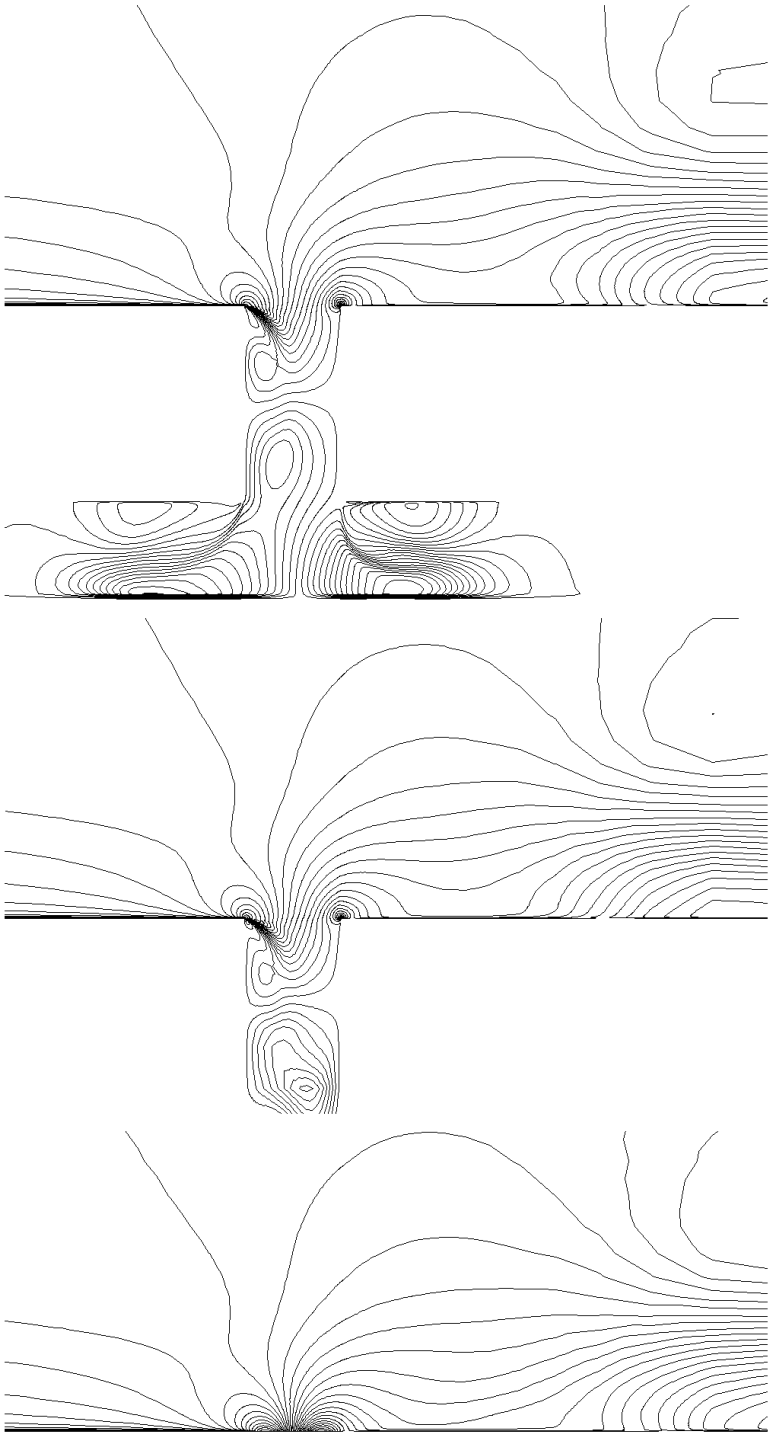

Figure 22: Iso-u contours for the cavity (top), slot (middle) and boundary (bottom) models, for $\Phi = \pi$ (500 Hz).

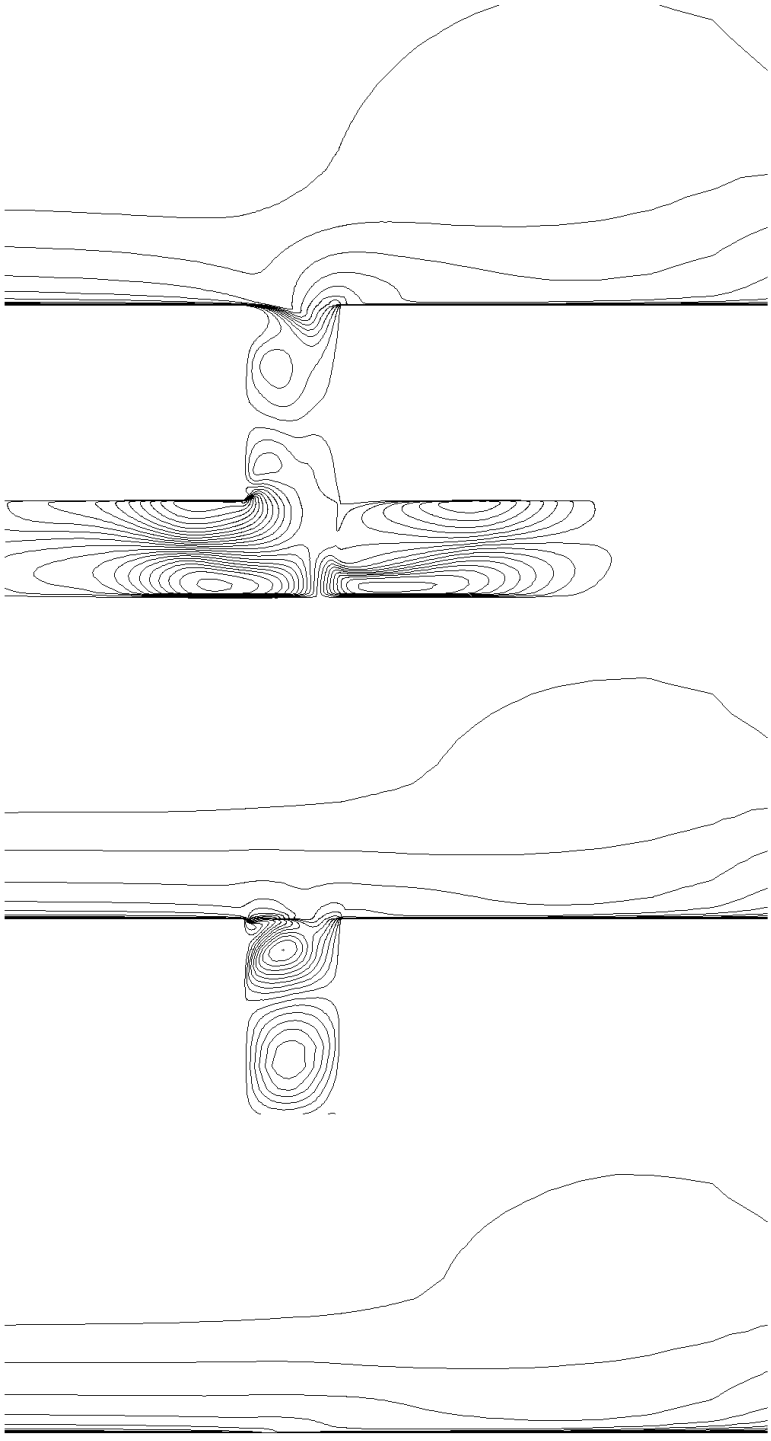

Figure 23: Iso-u contours for the cavity (top), slot (middle) and boundary (bottom) models, for $\Phi = 3\pi/2$ (500 Hz).

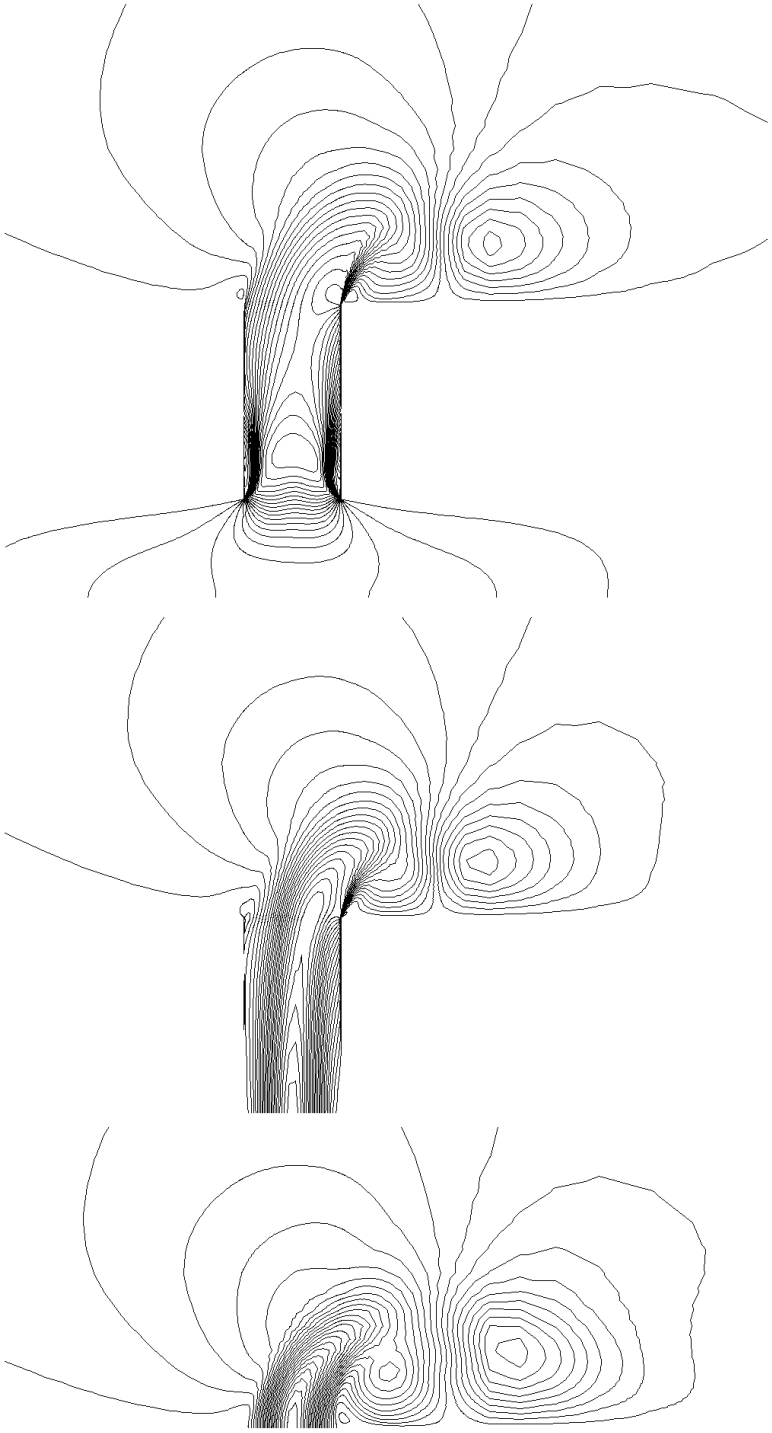

Figure 24: Iso-v contours for the cavity (top), slot (middle) and boundary (bottom) models, for $\Phi = 0$ (500 Hz).

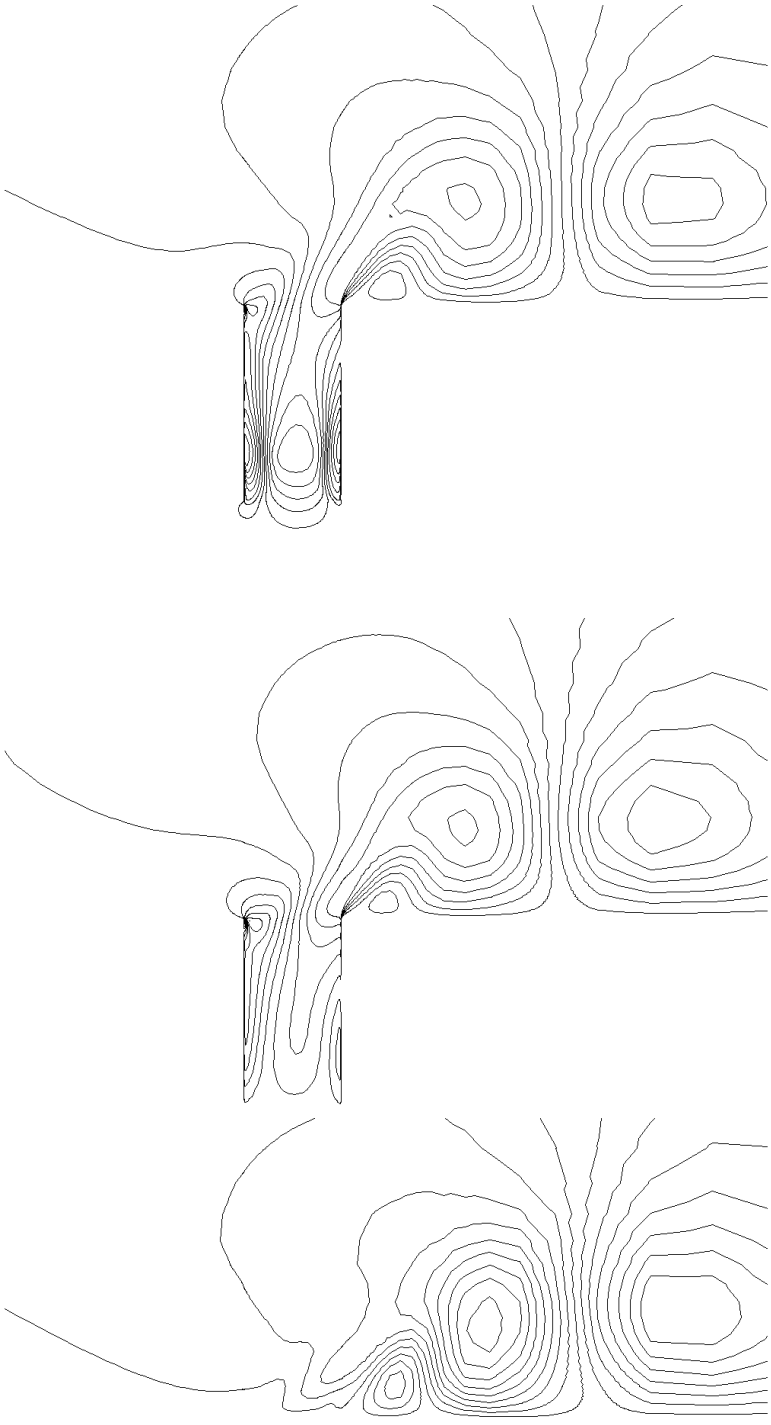

Figure 25: Iso-v contours for the cavity (top), slot (middle) and boundary (bottom) models, for $\Phi = \pi/2$ (500 Hz).

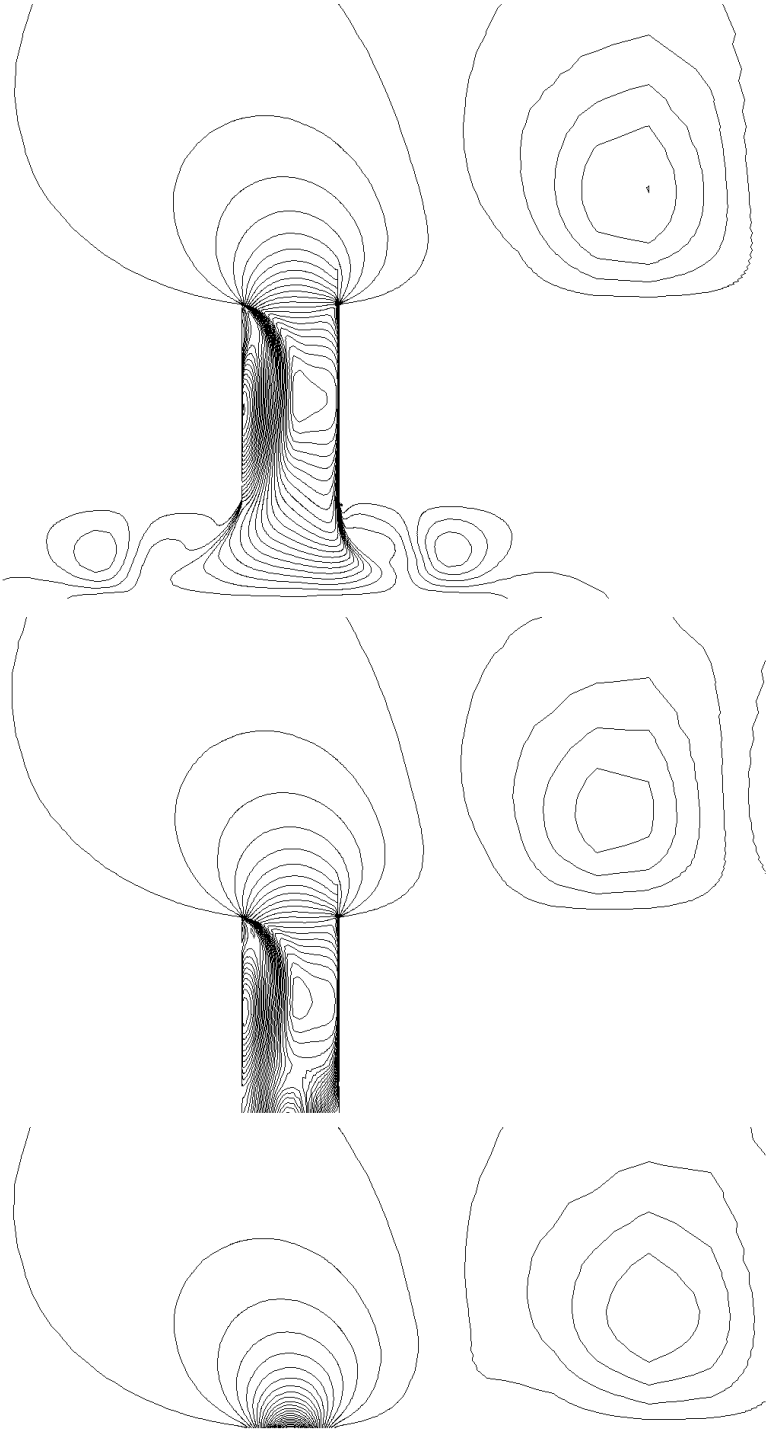

Figure 26: Iso-v contours for the cavity (top), slot (middle) and boundary (bottom) models, for $\Phi = \pi$ (500 Hz).

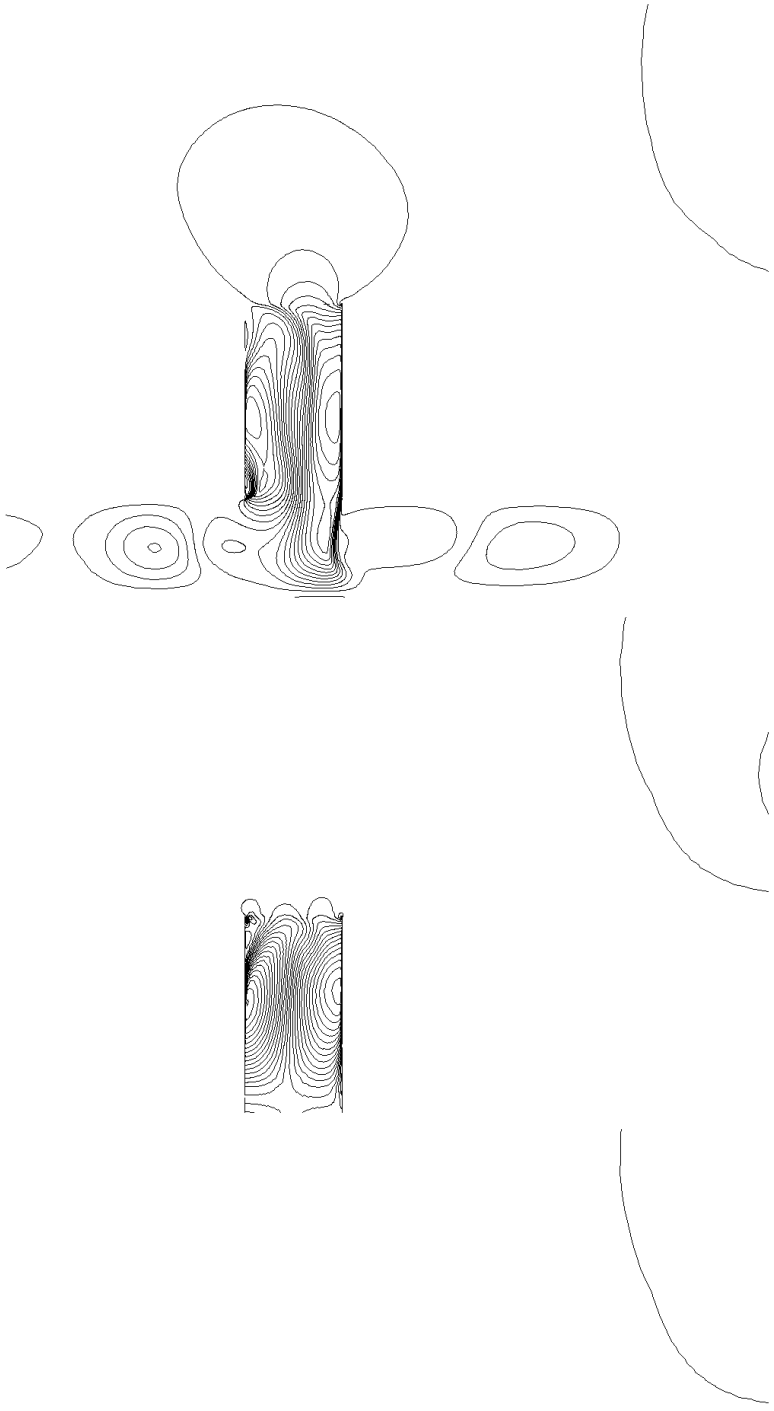

Figure 27: Iso-v contours for the cavity (top), slot (middle) and boundary (bottom) models, for $\Phi = 3\pi/2$ (500 Hz).

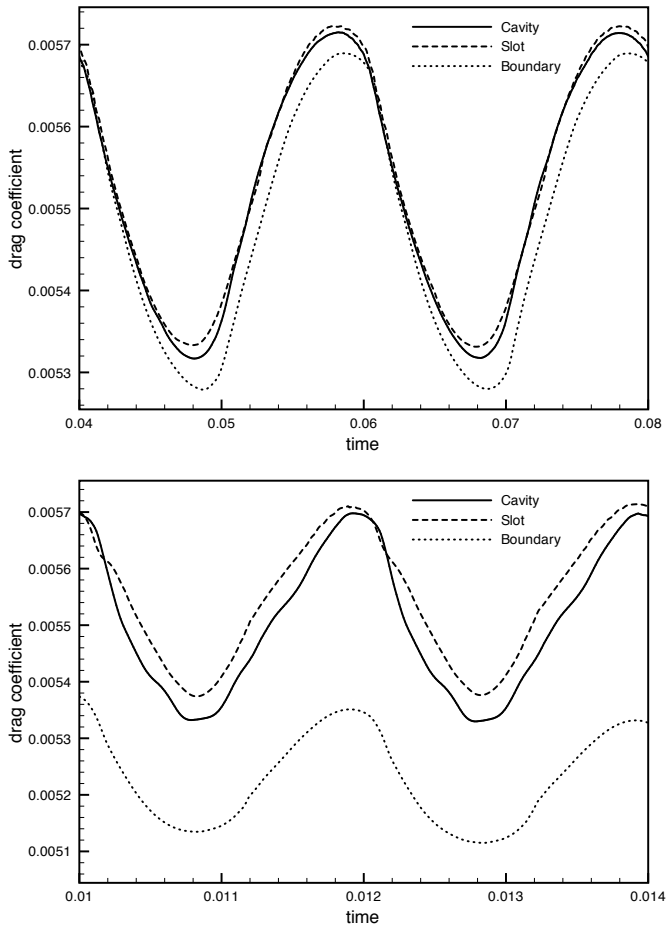

Figure 28: Time evolution of the drag coefficient, for the first actuation (top) and second actuation (bottom).

6 Impact of numerical parameters

In this section, we investigate the influence of some numerical parameters on the flow predicted. In the perspective of design optimization, we restrict this study to the boundary condition model for the actuation 1 and we use the drag coefficient as main comparison criterion. More precisely, we test the influence of the choice of the boundary condition type for the jet (weak vs. strong) and we measure the impact of the convergence criterion used for each time step. The SST $k-\omega$ turbulence closure is used here again.

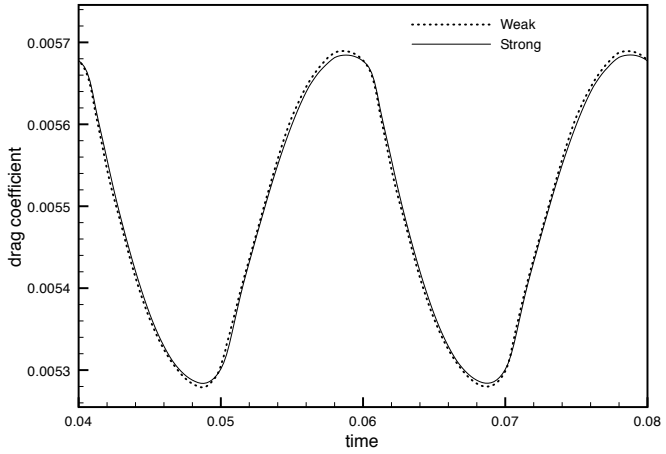

Figure 29: Time evolution of the drag coefficient, for weak and strong boundary conditions.

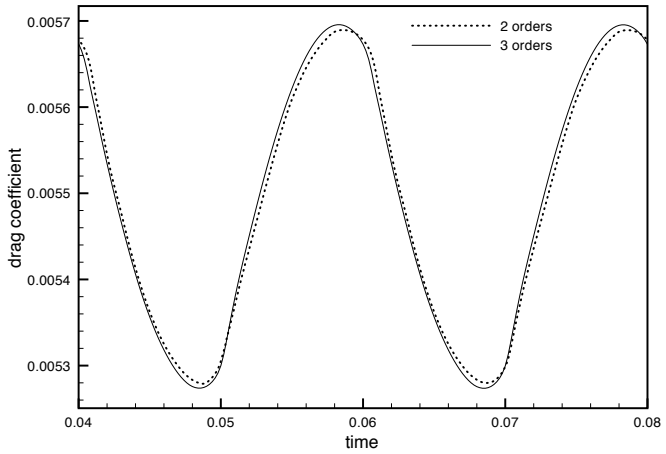

Figure 30: Time evolution of the drag coefficient, for different non-linear convergence criteria.

The evolution of the drag coefficient computed using weak and strong boundary conditions is depicted in Fig. (29). As seen, the discrepancy is not relevant. Indeed, the iterative process

carried out at each time-step makes the two approaches nearly identical.

Fig. (30) shows the same quantity, when different parameters are used as stopping criterion for the non-linear iterative process. Here again, the discrepancy is small, which indicates that the flow at each time-step is well converged.

7 Refinement study

To assess the computations, we finally perform a refinement study, by reducing the physical time step by a factor two, while applying a uniform grid refinement by a factor $\sqrt{2}$ in each direction, yielding a fine mesh counting 32010 vertices. The comparison of the time evolution of the drag coefficient for the two meshes is depicted in Fig. (31). As can be observed, the use of finer grid and time-step slightly modifies the drag coefficient value during the suction phase. However, the change is rather moderate. In particular, the time-averaged drag coefficient is not significantly affected by the refinement.

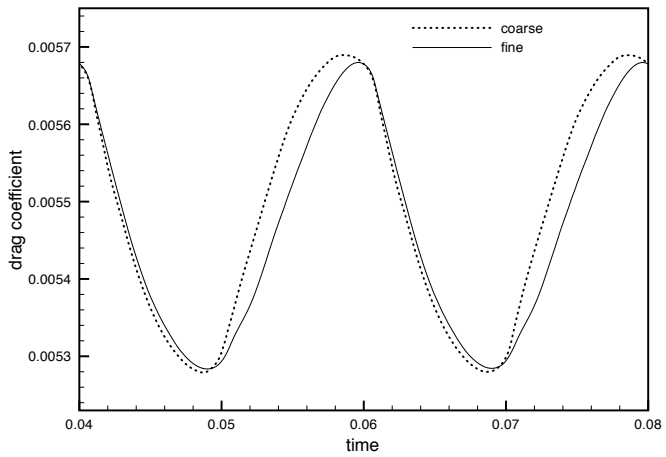

Figure 31: Time evolution of the drag coefficient, for two meshes.

8 Impact of turbulence closure

As the synthetic jet generates detached flows, it is of particular interest to compare the flows predicted by different turbulent closures. We consider for this study the SST $k-\omega$ from Menter and the Spalart-Allmaras closures, using the boundary model for both actuations.

The time evolution of the drag coefficient for the two closures is represented in Fig (32). As seen, the SST $k-\omega$ closure predicts a lower drag than the Spalart-Allmaras one, especially during the blowing phase and for the high-frequency actuation. Nevertheless, the discrepancy between these values has the same magnitude as that observed for the steady flow without actuation (about 10^{-4}).

Figs (33-40) show velocity contours for the two closures at some actuation phases (maximum blowing and maximum suction). One can notice that the flows are globally close to each other. It

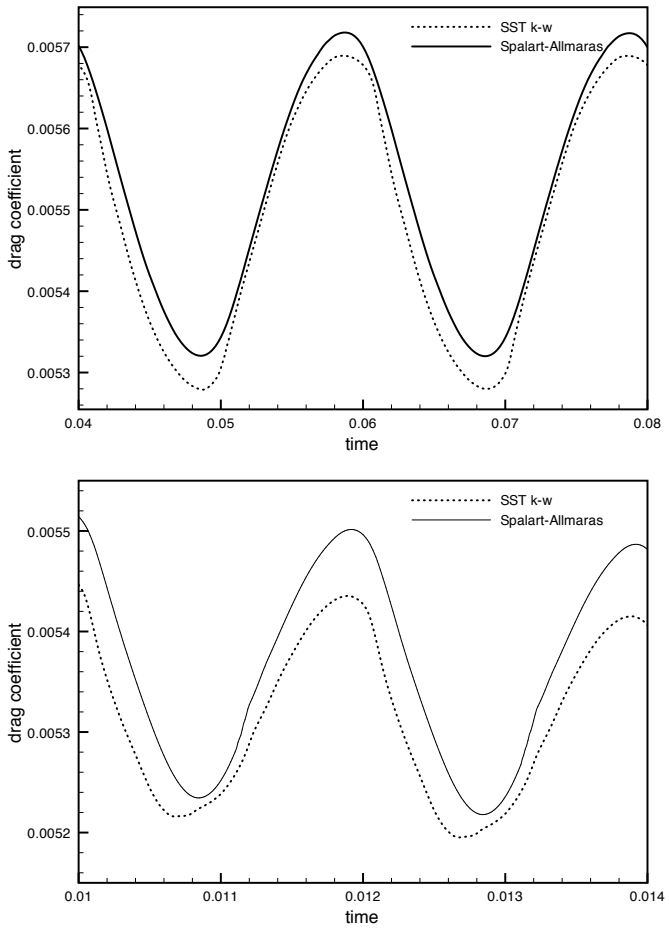

Figure 32: Time evolution of the drag coefficient for different turbulence closures, for the first actuation (top) and second actuation (bottom).

is confirmed that they differ mainly during the blowing phase, the SST $k-\omega$ closure generating a more vortical flow, with more intense gradients, than the Spalart-Allmaras one.

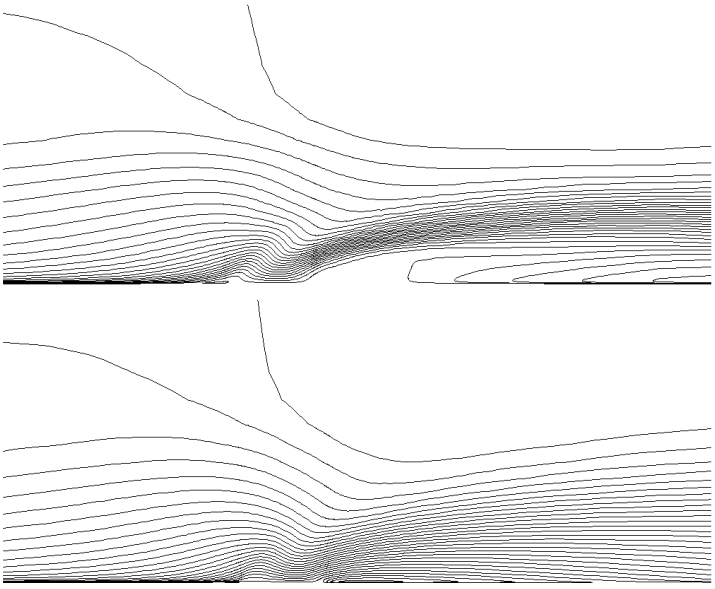

Figure 33: Iso-u contours for the SST $k-\omega$ (top) and Spalart-Allmaras (bottom) closures, for $\Phi = 0$ (50 Hz).

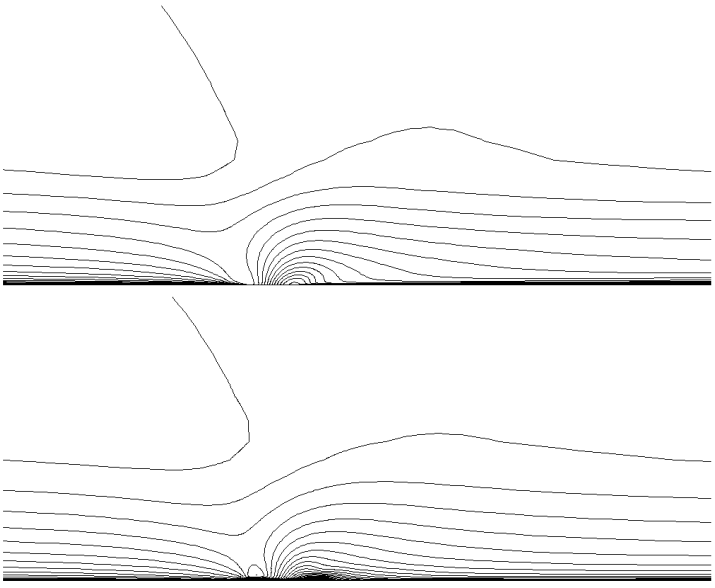

Figure 34: Iso-u contours for the SST $k-\omega$ (top) and Spalart-Allmaras (bottom) closures, for $\Phi = \pi$ (50 Hz).

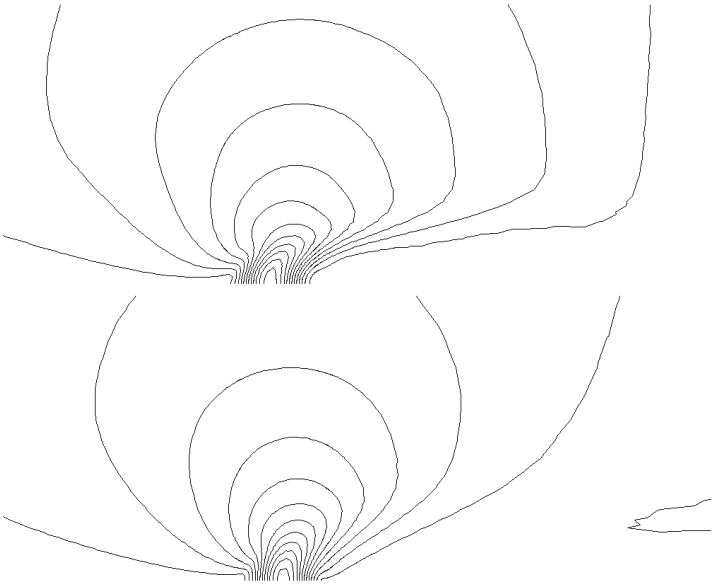

Figure 35: Iso-v contours for the SST $k-\omega$ (top) and Spalart-Allmaras (bottom) closures, for $\Phi = 0$ (50 Hz).

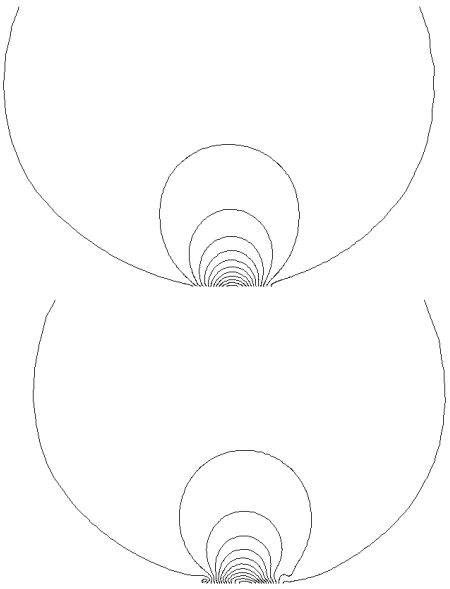

Figure 36: Iso-v contours for the SST $k-\omega$ (top) and Spalart-Allmaras (bottom) closures, for $\Phi = \pi$ (50 Hz).

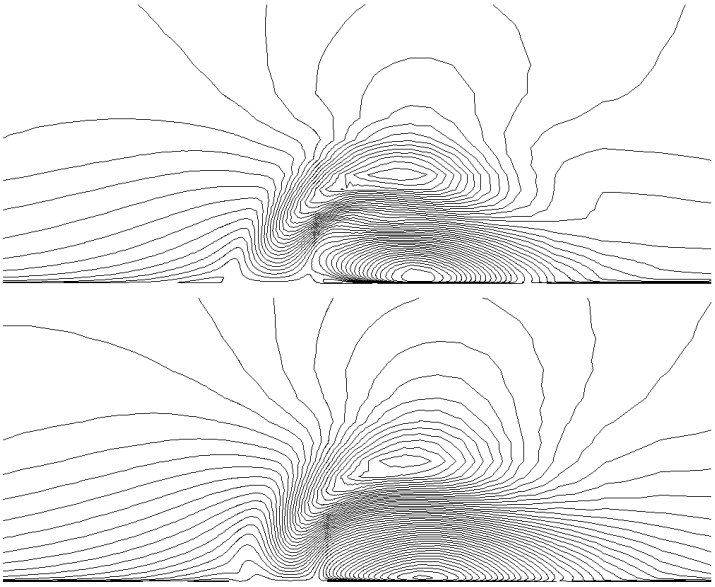

Figure 37: Iso-u contours for the SST $k-\omega$ (top) and Spalart-Allmaras (bottom) closures, for $\Phi = 0$ (500 Hz).

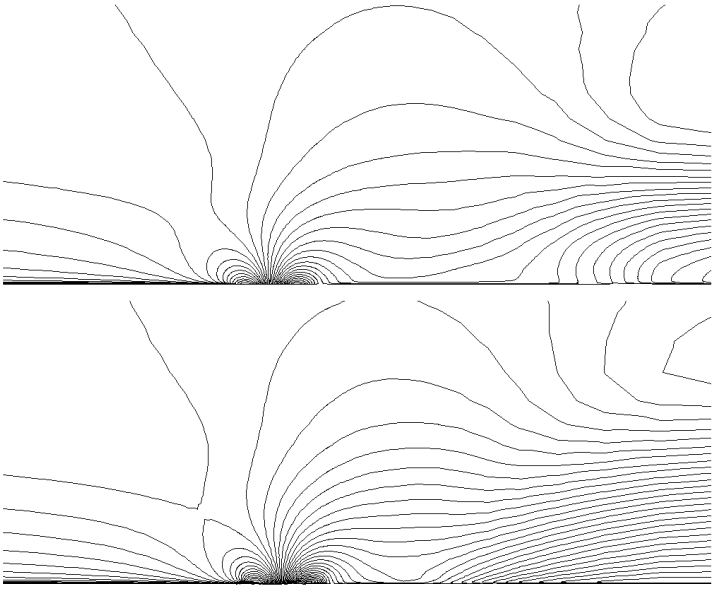

Figure 38: Iso-u contours for the SST $k-\omega$ (top) and Spalart-Allmaras (bottom) closures, for $\Phi = \pi$ (500 Hz).

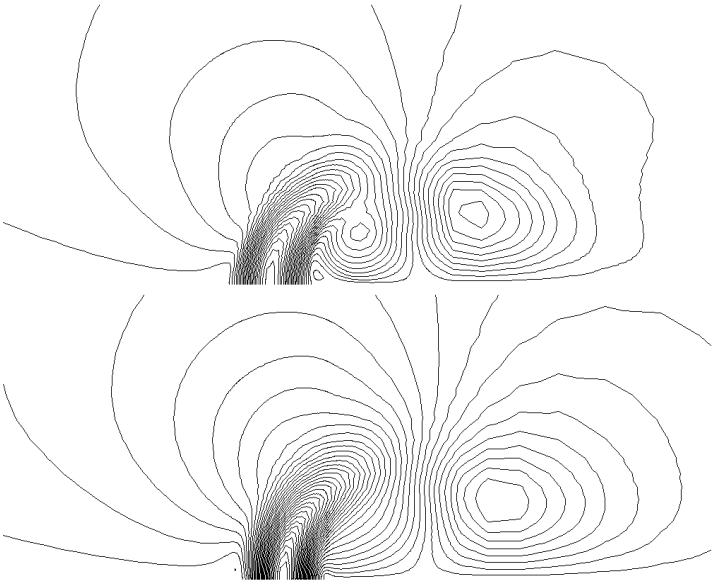

Figure 39: Iso-v contours for the SST $k-\omega$ (top) and Spalart-Allmaras (bottom) closures, for $\Phi = 0$ (500 Hz).

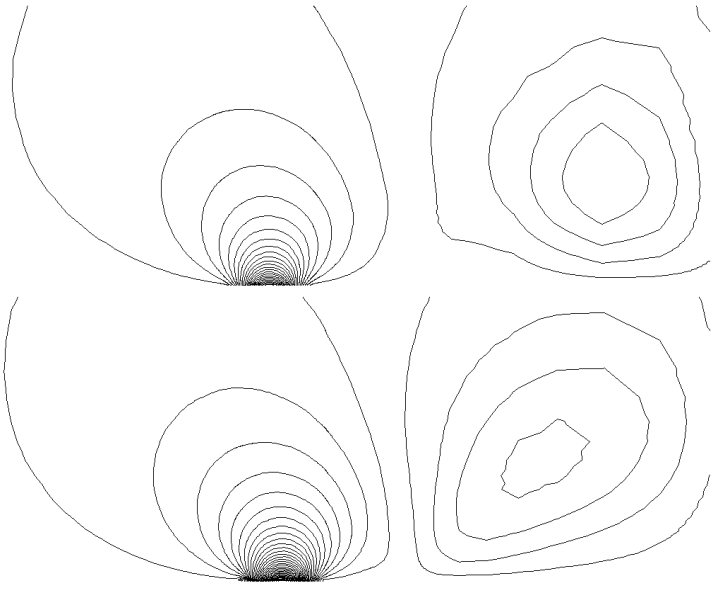

Figure 40: Iso-v contours for the SST $k-\omega$ (top) and Spalart-Allmaras (bottom) closures, for $\Phi = \pi$ (500 Hz).

9 Conclusion

The objective of the current study was to simulate a synthetic jet in a turbulent boundary layer flow, compare the flows predicted by some actuator models and assess the turbulence closures in this context. This study can be considered as a preparatory work before optimization of control parameters for more complex problems.

It has been found that the actuator model including the slot description is a satisfactory compromise between the complexity of including the whole cavity and the simplicity of using only a boundary condition. The numerical parameters (convergence criterion, grid size, time step, type of boundary condition) have been set to reasonable values for the problem considered.

Regarding the influence of turbulence closures, a moderate discrepancy between the Spalart-Allmaras and the SST $k-\omega$ closures has been reported, the latter generating a more intense flow at blowing. However, it would be interesting to consider more different models for future studies, such as non-linear algebraic stress models.

Acknowlegement

This study is supported by the 7th Framework Program of the European Union, project number 266326 "MARS".

References

[1] P. Batten, N. Clarke, C. Lambert, and M. Causon. On the choice of wavespeeds for the hllc Riemann solver. *SIAM J. Sci. Comput.*, 18(6):1553–1570, November 1997.

[2] M. Bergmann and L. Cordier. Optimal control of the cylinder wake in the laminar regime by trust-region methods and pod reduced-order models. *J. Comput. Physics*, 227(16), 2008.

[3] A. Carnarius, F. Thiele, E. Oezkaya, A. Nemili, and N. Gauger. Optimization of active flow control of a naca 0012 airfoil by using a continuous adjoint approach. In *European Congress on Computational Methods in Applied Sciences and Engineering, Vienna, Austria*, 2012.

[4] J. Dandois. *Contrôle des décollements par jet synthétique*. PhD thesis, University Paris VI, 2007.

[5] J. Dandois, E. Garnier, and P. Sagaut. Unsteady simulation of synthetic jet in a crossflow. *AIAA Journal*, 44(2), 2006.

[6] A. Dervieux and J.-A. Désidéri. Compressible flow solvers using unstructured grids. INRIA Research Report 1732, June 1992.

[7] J.F. Donovan, L.D. Kral, and A.W. Cary. Active flow control applied to an airfoil. AIAA Paper 98–0210, January 1998.

[8] R. Duvigneau, A. Hay, and M. Visonneau. Optimal location of a synthetic jet on an airfoil for stall control. *Journal of Fluid Engineering*, 129(7):825–833, July 2007.

[9] R. Duvigneau and M. Visonneau. Optimization of a synthetic jet actuator for aerodynamic stall control. *Computers and Fluids*, 35:624–638, July 2006.

[10] R. P. Dwight. *Efficiency improvements of RANS-based analysis and optimization using implicit and adjoint methods on unstructured grids*. PhD thesis, University of Manchester, 2006.

[11] J.A. Ekaterinaris. Active flow control of wing separated flow. ASME FEDSM'03 Joint Fluids Engineering Conference, Honolulu, Hawai, USA, July 6-10, 2003.

[12] J.L. Gilarranz, L.W. Traub, and O.K. Rediniotis. Characterization of a compact, high power synthetic jet actuator for flow separation control. AIAA Paper 2002–0127, September 2002.

[13] J. W. He, R. Glowinski, R. Metcalfe, A. Nordlander, and J. Periaux. Active control and drag optimization for flow past a circular cylinder: I. oscillatory cylinder rotation. *Journal of Computational Physics*, 163(1):83 – 117, 2000.

[14] T. Kloczko, C. Corre, and A. Beccantini. Low-cost implicit schemes for all-speed flows on unstructured meshes. *International Journal for Numerical Methods in Fluids*, 58(5):493–526, October 2008.

[15] L.D. Kral, J.F. Donovan, A.B. Cain, and A.W. Cary. Numerical simulation of synthetic jet actuators. In *AIAA Paper 97-1824*, 1997.

[16] F.R. Menter. Two-equation eddy-viscosity turbulence models for engineering applications. *AIAA Journal*, 32(8), 1994.

[17] A. Seifert, A. Darabi, and I. Wygnanski. Delay of airfoil stall by periodic excitation. *AIAA Journal*, 33(4):691–707, July 1996.

[18] B. Smith and A. Glezer. Vectoring and small-scale motions effected in free shear flows using synthetic jet actuators. In *AIAA Paper 97-0213*, 1997.

[19] A. Zymaris, D. Papadimitriou, K. Giannakoglou, and C. Othmer. Optimal location fo suction or blowing jets using the continuous adjoint approach. In *European Congress on Computational Methods in Applied Sciences and Engineering ECCOMAS 2010 Lisbon*, 2010.

Contents

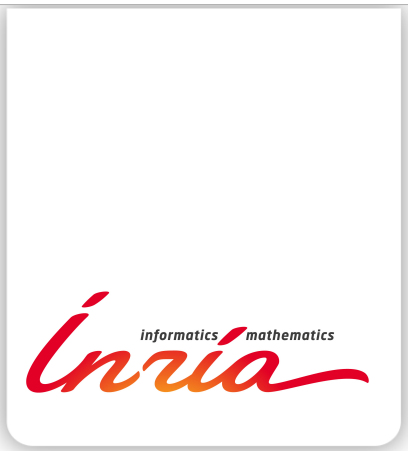

RESEARCH CENTRE
SOPHIA ANTIPOLIS – MÉDITERRANÉE

2004 route des Lucioles - BP 93
06902 Sophia Antipolis Cedex

Publisher
Inria
Domaine de Voluceau - Rocquencourt
BP 105 - 78153 Le Chesnay Cedex
inria.fr

ISSN 0249-6399